Direct wavefront sensing in adaptive optical microscopy using backscattered light

Saad A. Rahman[1] and Martin J. Booth[1,2,*]

[1]Department of Engineering Science, University of Oxford, Parks Road, Oxford, OX1 3PJ, UK

[2]Centre for Neural Circuits and Behavior, University of Oxford, Mansfield Road, Oxford, OX1 3SR, UK

*Corresponding author: martin.booth@eng.ox.ac.uk

Received 3 May 2013; revised 3 July 2013; accepted 5 July 2013;
posted 10 July 2013 (Doc. ID 189946); published 30 July 2013

Adaptive optics has been used to compensate the detrimental effects of aberrations in a range of high-resolution microscopes. We investigate how backscattered laser illumination can be used as the source for direct wavefront sensing using a pinhole-filtered Shack–Hartmann wavefront sensor. It is found that the sensor produces linear response to input aberrations for a given specimen. The gradient of this response is dependent upon experimental configuration and specimen structure. Cross sensitivity between modes is also observed. The double pass nature of the microscope system leads in general to lower sensitivity to odd-symmetry aberration modes. The results show that there is potential for use of this type of wavefront sensing in microscopes.

OCIS codes: (010.7350) Wave-front sensing; (180.1790) Confocal microscopy; (180.5810) Scanning microscopy; (220.1080) Active or adaptive optics.

http://dx.doi.org/10.1364/AO.52.005523

1. Introduction

Optical microscopes are widely used in the biological sciences to image cellular structures and function. Laser scanning methods, such as confocal or multiphoton microscopes, are particularly useful as they provide 3D images of thick specimens. The effectiveness of such microscopes is compromised by specimen-induced aberrations, so adaptive optics has been employed to compensate for these aberrations through the introduction of a conjugate aberration using an adaptive element, such as a deformable mirror (DM) [1].

Aberrations can be measured either using direct wavefront sensing or indirect sensorless optimization methods. Sensorless optimization uses image information to determine the specimen-induced aberration from a sequence of measurements. This has successfully been demonstrated in several adaptive microscope applications [2,3]. Recent work has shown that direct wavefront sensing can also be employed. For this to be effective, a method is needed to ensure that only light from the focal region contributes to the aberration measurement. Several implementations have used fluorescence emission for aberration measurement. In two-photon excitation fluorescence microscopes, fluorescence is only generated in the focal spot, which can be used as the source for a wavefront sensor [4,5]. Another approach involves the placement of small fluorescent beads in the specimen that can act as point sources for wavefronts that are detected by a Shack–Hartmann wavefront sensor (SHWFS) [6,7].

For weakly fluorescent or sensitive specimens, it would be desirable to use backscattered illumination light, whose intensity is often orders of magnitude greater than the resulting fluorescence. However, aberrations encountered in backscattered light can depend upon the specimen structure and the resulting measurements can be ambiguous. For example, reflection by a planar mirror in the focus of the

1559-128X/13/225523-10$15.00/0

microscope would result in a doubling of even-symmetry aberrations, such as astigmatism or spherical aberration, whereas odd-symmetry aberrations, such as coma, are cancelled out [8,9]. Scattering from isolated point objects would, however, result in the correct detection of aberrations. Intermediate-sized objects with dimensions similar to the wavelength would exhibit more complex scattering characteristics.

One method has used backscattered illumination light and coherence gating to ensure that the wavefront sensor only responded to light scattered from the focal region [10]. This approach is only possible with low-coherence illumination and requires a complicated interferometric arrangement. Alternatively, a pinhole can be used to exclude out-of-focus light, in a similar way to the pinhole used in a confocal microscope. The pinhole has the additional advantage of smoothing the light field that reaches the wavefront sensor pupil. The size of the pinhole must be carefully chosen to provide a compromise between spatial selectivity and the degree of smoothing. Such an arrangement has been used for fluorescence-based wavefront sensing in a confocal microscope, but not using backscattered illumination light [11,12].

In this paper, we expand upon previous preliminary work [13] and present experimental data illustrating the effectiveness of direct sensing using a pinhole-filtered SHWFS for mirror and scattering specimens. The effects of different pinhole sizes on the measured aberrations are determined, as are the effects of different scattering structures. We also investigate the differing sensitivity of the SHWFS to even- and odd-symmetry aberration modes and measurements. This effect, arising from the dual pass nature of the optical system, has been investigated previously for ophthalmic applications, but this is the first detailed investigation of these phenomena in high numerical aperture microscopy [8,9].

2. Experimental System

Figure 1 shows a simplified schematic of the wavefront sensing system used for the experimental measurements. Light of wavelength 633 nm from a helium neon laser was expanded by a combination of lenses to form a beam that illuminated the membrane DM (Flexible Optical, Netherlands). The default position of the DM was set at approximately half of its maximum deflection. The illuminating beam was set to be divergent, hence compensating for the DM curvature arising from the default shape of the mirror. The membrane mirror, which allows correction of low-order optical aberrations, has a 15 mm diameter, Al-coated circular mirror membrane, and its 37 electrodes are arranged in a hexagonal structure within a 12 mm diameter circle. Experimentally, it was found that optimum reproduction of Zernike modes was achieved when using around 10 mm diameter active aperture on the DM. Light reflected by the DM was passed through a 4*f*

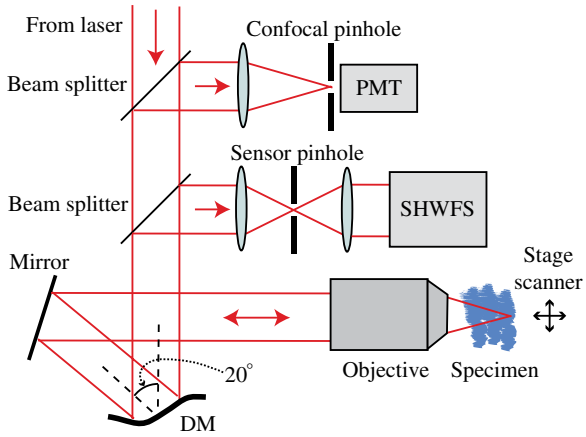

Fig. 1. Schematic of the microscope wavefront sensing system. Several optical elements have been omitted for clarity. Arrows show the light propagation direction in the illumination and detection paths.

system and focused by a water immersion objective lens (Zeiss, 63×, 1.2 NA) to probe a specimen that was placed on a piezo scanning stage, which allowed raster scanning of the specimen. Light backscattered from the specimen was collected by the same objective lens, then was incident on the DM once more in the detection path. The light reflected by the DM was coupled off by a beam splitter and passed through a 4*f* lens system. First, this 4*f* system served to demagnify the beam so that it can be picked up completely by the CCD camera on the SHWFS (Thorlabs, WFS150, with custom software). Second, it was used to collimate the convergent beam reflected by the DM. Third, the lens system was used to focus the light through a pinhole, which performed the essential tasks of filtering out light from out-of-focus regions and smoothing of the light distribution incident on the SHWFS.

A range of pinholes with different diameters was used. The pinhole excluded out-of-focus light in a similar manner to the pinhole used in a confocal microscope. The effects of the pinhole size on the confocal microscope have been well studied [14,15]. Optimal axial sectioning is obtained for a vanishingly small pinhole, although pinhole diameters up to around 70% of the first zero of the Airy pattern provide essentially equivalent sectioning with the additional benefit of increased signal. For larger pinhole sizes, the sectioning depth increases in an approximately linear manner. For the pinhole filtered SHWFS, an increase in pinhole size similarly increases the axial depth from which scattered light contributes to the sensor measurement.

In an adaptive microscope, the specimen's refractive index structure would induce similar aberrations in both the illumination and detection paths. In order to simulate specimen-induced aberrations, the DM was used to introduce individual aberration modes simultaneously into both paths. This configuration models very closely the effect of specimens, with the restriction that only aberrations with the

capabilities of the DM are included. The control signals required to generate Zernike polynomial modes were obtained through calibration of the system using the SHWFS. Linearized deflection of the mirror surface was achieved by using actuator drive voltages that were proportional to the square root of the control signal [16]. The amplitude of the Zernike modes was swept from −0.6 to 0.6 units, in steps of 0.2 units, where one unit corresponds to a root mean square phase of 1 rad. Higher amplitudes caused the DM electrode voltage to saturate for some modes. As the backscattered light incident on the SHWFS had complex structure like a speckle pattern, scanning and averaging was necessary in order to obtain reliable measurements. For each applied amplitude of the Zernike modes, averaging was achieved, first, via long exposure of the specimen while it was being scanned. Second, several of the resulting pupil images were recorded by the SHWFS camera. The Zernike coefficients were estimated from the averaged pupil image by calculating the centroid of each Hartmann spot and using the least-squares method of Southwell [17]. The exposure time and number of images averaged were selected so as to achieve a uniform pupil intensity at the SHWFS, which in turn produced steady coefficient measurements. In order to illustrate the variability between measurements, several sets of the coefficients were recorded in this way. The multiple readings were used to calculate the mean and standard deviation of the data so as to provide an indication of the repeatability of wavefront sensing for a given scenario.

The effects of scattering in the specimen and spatial filtering by the detector pinhole create dark regions in the pupil that correspond to missing spots in the Hartmann spot pattern. The nonuniform intensity also gives rise to brighter regions in the pupil that may cause saturation of the CCD sensor, which can lead to errors in the calculation of the spot centroid. These missing or corrupted centroid measurements inevitably introduce errors into the wavefront measurements. The control software was programmed to use the reference (i.e., undeflected) spot position where a spot was missing or saturated, yielding a zero local phase gradient.

3. Measurements for Different Specimen Structures

The system described in the previous section was used to investigate wavefront sensing using backscattered light in different specimens. In this section, we present results illustrating the effectiveness of aberration measurements using a range of specimens, ranging from a specular mirror-like specimen and scattering structures consisting of beads and natural specimens.

It can be easily shown that a specular specimen, such as a mirror, yields twice the induced even-symmetry aberrations and no odd-symmetry aberrations in a dual pass setup, such as the confocal microscope. To demonstrate this phenomenon, a mirror was placed on the stage of the dual pass wavefront sensing system of Fig. 1. An aperture of 10 mm diameter was illuminated on the DM. The reflected beam was imaged to fill exactly the back aperture of the objective lens. The light reflected back by the mirror specimen and off the DM was demagnified to 4.1 mm diameter to form the input to the SHWFS. As a result, a total of 540 lenslets were illuminated and used by the SHWFS for aberration estimation. Figure 2 shows the measurements made by the SHWFS using the mirror specimen with the introduction of even symmetry aberration modes (astigmatism and spherical) by the DM. A range of pinholes with different diameters was used to provide axial selectivity and smoothing for the SHWFS. The diameter of the aberration-free Airy disc (referred to as the Airy unit) at the position of the SHWFS pinhole was 30.9 μm. For the astigmatism mode, it can be seen that the measurements made with the 200, 300, and 600 μm pinholes were almost identical to the measurements made without a pinhole in place. The measured aberration amplitude was approximately twice that of the induced aberration, as predicted by theory. The asymmetry in these latter plots is due to residual aberrations. For the smaller pinhole sizes of 100 and 50 μm, there was deviation from the ideal measurement. For the spherical aberration mode, the measurements were more sensitive to effects of the pinhole, with the gradient of the response decreasing noticeably as the pinhole diameter was reduced below 600 μm. The deviation of these gradients from the ideal is due to the spatial filtering effect of the pinhole. The spatial filtering caused smoothing of the pupil phase and, for regions with large phase gradient, a reduction in intensity. These dark pupil regions led to missing SHWFS spots which affected the measured aberration. A comparison of this effect for the Z_5 and Z_{11} modes is shown in Figs. 3(a) and 3(b). The greater sensitivity of Z_{11} to this phenomenon can be explained by consideration of the phase gradients of the different modes [Fig. 3(c)]. In a ray optics approximation, the gradient of the wavefront is proportional to the deflection of the corresponding ray in the focal plane from the optic axis. The larger gradients of the Z_{11} mode for a given amplitude mean that more light is filtered by the pinhole and more spots are lost from the SHWFS pattern.

Equivalent measurements were also taken for low-order, odd-symmetry modes, such as coma. In this case, the experimental measurements showed negligible detection of coma with the mirror specimen. This is entirely in agreement with theoretical modelling, which shows that the inversion of symmetry on reflection in the focus causes cancellation of odd aberration modes. A summary of the sensor response gradients to each Zernike mode for the 100 and 300 μm pinholes and with no pinhole is shown in Fig. 4. This figure (and subsequent figures) shows two quantities for each aberration mode. The first quantity is the sensitivity, denoted $|a_{i,i}|$ and shown as a black bar, which is the gradient of the sensor response to the mode i induced by the DM. The second

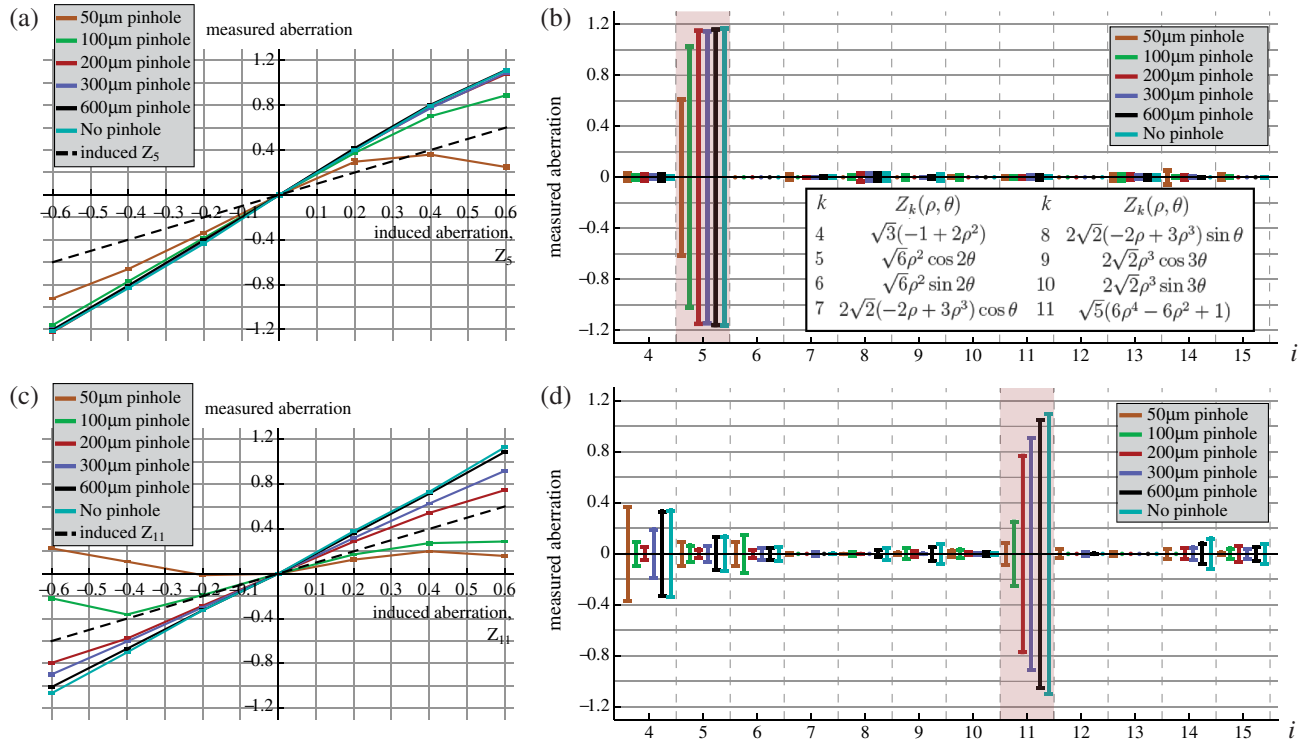

Fig. 2. SHWFS measurements of the DM-induced even aberration modes, (a, b) Z_5 (astigmatism) and (c, d) Z_{11} (spherical), for the mirror specimen. (a, c): Measured aberration amplitude as a function of induced aberration amplitude. (b, d): Maximum measured range of all Zernike modes when ±0.6 rad (rms) of Z_5 or Z_{11} was induced, showing crosstalk between modes. The inset in (b) shows the definition of the Zernike modes.

quantity is the modal crosstalk, denoted $|\{a_{i\neq k}\}|$ and shown as a gray bar, which is the root mean square sum of the other detected aberration coefficients when mode i was induced by the DM. An ideal measurement would therefore correspond to $|a_{i,i}| = 1$ and $|\{a_{i\neq k}\}| = 0$. The ratio $|a_{i,i}|/|\{a_{i\neq k}\}|$ quantifies the purity of the coefficient measurement.

To test the behavior of the dual pass wavefront sensing system in a scattering sample, a model specimen was created using polystyrene beads of 200 nm diameter. A suitably diluted suspension of distilled water and beads was mixed with powdered gelatin and then allowed to set between a glass slide and a glass coverslip, resulting in the beads being fixed in a three-dimensional distribution. The resulting specimen exhibited significant scattering from the dense arrangement of beads, as illustrated in the confocal microscope image (Fig. 5). As a large reflection was created by the interface between the glass coverslip and the (water-based) gelatin, it was important to be able to focus several tens of micrometers into the specimen to ensure that the light entering the SHWFS was scattered from the beads. The SHWFS pinhole ensured that only light scattered from near the focal region could contribute significantly to the aberration measurement.

Figure 6 shows the response of the SHWFS to even-symmetry aberration modes (Z_5 astigmatism

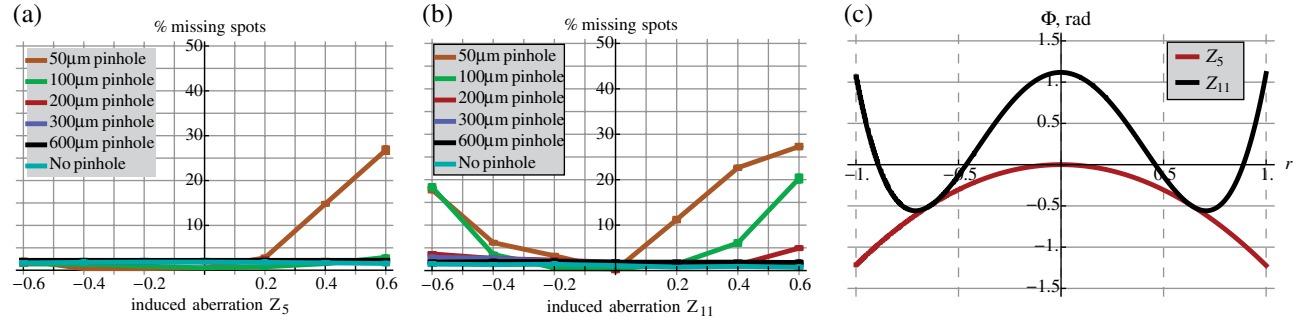

Fig. 3. Percentage of missing SHWFS spots for different pinhole sizes for different amplitudes of modes (a) Z_5 and (b) Z_{11}. (c) Cross sections through the Zernike modes Z_5 and Z_{11} with RMS amplitude 0.5 rad for $\theta = \pi/2$. The average gradient of Z_{11} is higher, leading to more light loss at the pinhole and more missing spots in the SHWFS.

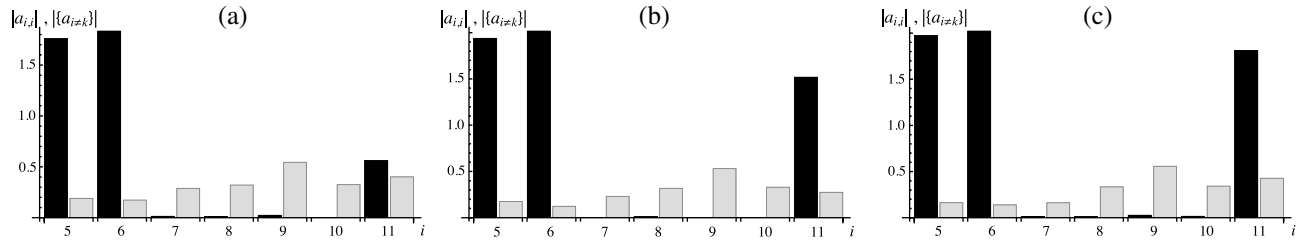

Fig. 4. Sensitivity to the induced Zernike mode of index i (black) and the total rms crosstalk sensitivity measured in other modes (gray) for Zernike modes 5 to 11 using the mirror specimen for (a) 100 μm diameter pinhole, (b) 300 μm pinhole, and (c) no pinhole.

and Z_{11} spherical) for the scattering bead specimen. Note that measurements for Z_6 (astigmatism) were also taken and were found to be similar to those obtained for the homologous mode Z_5. In this case, pinholes of 200, 300, and 600 μm diameter were used. It was observed that the responses to each mode were approximately linear, although the gradient was considerably lower than one in each case. The gradient of the response was also dependent upon the pinhole size and differed between the astigmatism and spherical modes.

Figure 6 shows the response of the SHWFS to the odd aberration modes Z_7 (coma) and Z_9 (trefoil) for the scattering bead specimen. Similar results were also obtained for the modes Z_8 and Z_{10}, respectively. Again, an approximately linear relationship between the induced and measured aberration was also observed. In these cases, however, the gradient was much smaller than that seen for the even modes. Dependence of the gradient on the pinhole size was also observed. A summary of the sensor response to each Zernike mode for the scattering bead specimen is shown in Fig. 7. The large degree of crosstalk could be caused by a combination of multiple scattering and the nonpoint-like nature of the 200 nm beads, which would both affect the SHWFS measurements.

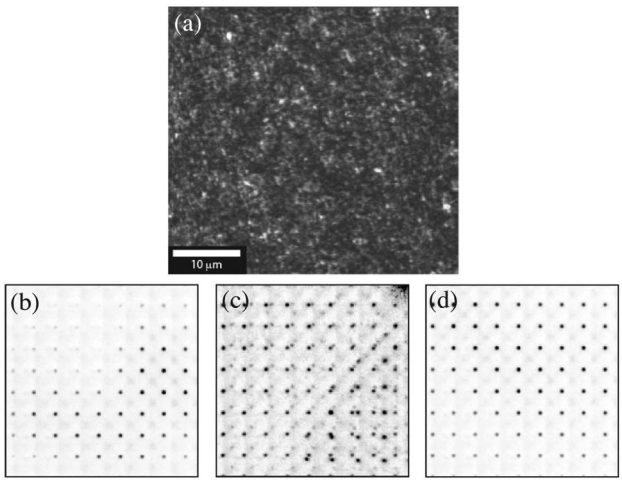

Fig. 5. (a) Confocal reflection microscope image of the 200 nm bead specimen. (b–d) SHWFS spot patterns using light backscattered from the sample 200 nm beads. A subregion of the pupil is shown. (b) Stationary specimen using a 200 μm pinhole, showing significant intensity variation across pupil. (c) Scanning and frame averaging with no pinhole, showing near uniform intensity but with out-of-focus light causing secondary spots within each subaperture domain. (d) Scanning and averaging, using a 200 μm pinhole, showing greater uniformity and no secondary spots.

A sample of artificial collagen was immersed in water and placed between a cover glass and microscope slide. This was chosen as the matrix of collagen fibrils scatter light in a different manner to beads and so provide a further test of wavefront sensing using light scattered from different specimens. Figure 8 shows a confocal reflection microscope image of the collagen sample, indicating strong scattering. Measurements were taken in the same manner as for the bead specimen. Scanning was performed over a region of approximately 50 μm square. As was observed for the bead specimen, the sensor response to Zernike modes was predominantly linear in all cases, although the gradient was dependent upon the pinhole size and is different between modes. The gradients observed for all modes 5 to 11 are shown in Fig. 9. As with the bead specimen, the measurements showed that the even aberration modes ($i = 5$, 6) were detected more efficiently than odd modes ($i = 7$ to 10). It was also observed that the sensitivity was in general higher than the corresponding values using the bead specimen.

Further measurements were taken from a specimen of 100 nm diameter gold beads suspended in gelatin. In this case, the specimen was sparsely populated with beads, such that the wavefront measurements were taken by scanning over a single bead. The sensitivity and crosstalk measured for modes 5 to 11 are shown in Fig. 10. The sensor response for this specimen shows similar characteristics for both the even and odd modes, which should be expected for scattering from point-like objects. This is in contrast to the measurement from the polystyrene beads and collagen, where the response to odd modes was lower. However, the measured coefficients were all lower than those for the induced aberration. The lower sensitivity to mode 11 (spherical) for the larger pinhole is attributed to an anomalous measurement; we note that significant defocus was detected in this case, indicating that an axial displacement of the bead had led to filtering of light illuminating the outer regions of the SHWFS.

4. Measurements for Different Optical Configurations

The light detected by the SHWFS can be backscattered by various specimen structures, which may

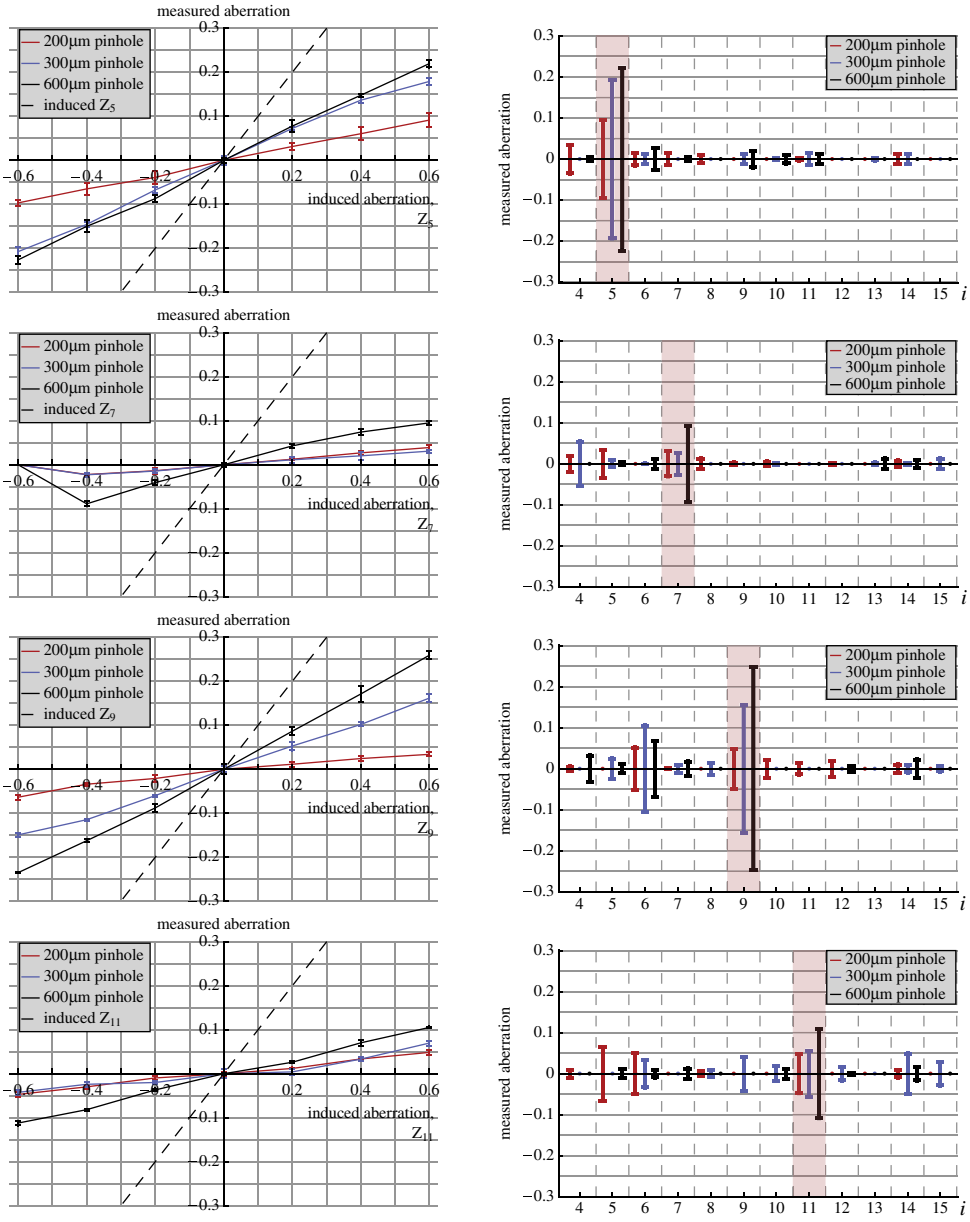

Fig. 6. SHWFS measurements of the even aberration modes Z_5 (astigmatism) and Z_{11} (spherical) and the the odd aberration modes Z_7 (coma) and Z_9 (trefoil) for the specimen of 200 nm diameter beads suspended in gelatin. Left: Measured aberration amplitude as a function of induced aberration amplitude. Right: Maximum measured amplitude of all modes, showing modal cross talk.

encompass specular reflections from locally flat interfaces, scattering by point-like features, and scatter from other intermediate structures. As indicated by theory and backed up by the measurements for the mirror and gold bead specimen (Figs. 4 and 10), the light scattered from smaller objects is likely to

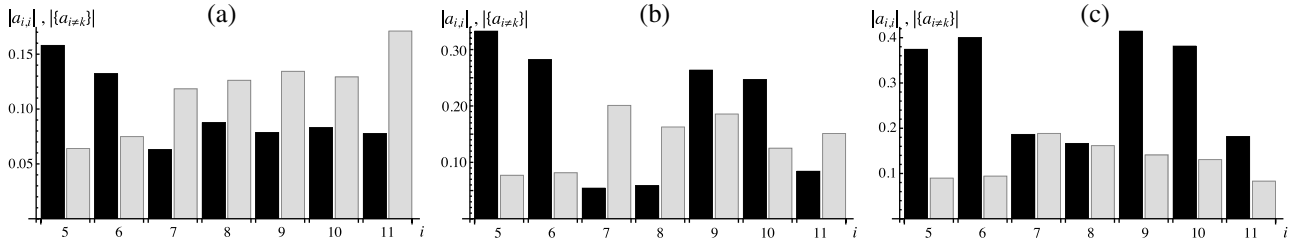

Fig. 7. Sensitivity (black) and crosstalk (gray) for Zernike modes 5 to 11 using the specimen of 200 nm diameter beads in gelatin with (a) 200 μm diameter pinhole, (b) 300 μm pinhole, and (c) 600 μm pinhole.

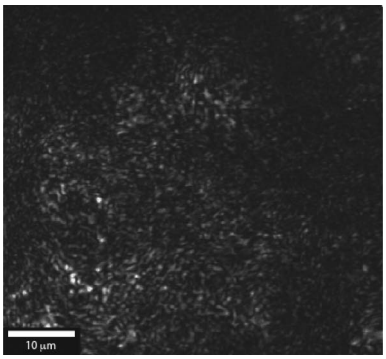

Fig. 8. Confocal reflection microscope image of the artificial collagen specimen.

provide more accurate measurements than those from larger structures. The separation of scattering from specular reflections should therefore improve the purity of the coefficient measurements. We have investigated two optical configurations to achieve this: asymmetric illumination and detection and polarization filtering.

A. Asymmetric Illumination and Detection

The results presented in previous sections used illumination that filled the full aperture of the objective lens. If the illumination is instead restricted to a smaller NA by underfilling the objective pupil, then specular components of the reflection would be confined to a limited region of the detection pupil. In contrast, scattered light would be distributed across the whole of the detection pupil. Aberration measurements using asymmetric illumination and detection, where the NA of the illumination beam is much lower than the NA of the detection path, might therefore be more sensitive to the scattered light from small objects. This asymmetric dual pass method has been shown in ophthalmic research of the human eye to produce better readings of both even and odd aberration modes [18,19].

Figure 11 shows results comparing symmetric and asymmetric illumination and detection. The optical system was modified so that the illumination NA was reduced to approximately 0.096, while the detection NA was maintained at 1.2. The response to odd aberration modes ($i = 7$ to 10) is higher for the asymmetric case, whereas the response to the even modes is slightly lower. This corresponds to the expectation that the asymmetric case should yield better sensitivity to odd modes, although the difference in sensitivity is small.

It should be noted that the asymmetric illumination configuration causes the spots at the center of the SH pattern to be saturated. The wavefront reconstruction scheme replaced these saturated measurements with a zero-phase gradient. This approximation would have the effect of reducing the measured coefficients compared to the symmetric case, where there was no saturation.

B. Polarization Filtering

Light reflected by a specular specimen in the focal region of a high NA objective lens will maintain the same polarization state as the illumination. However, when light is scattered by a small object in the focus, a degree of depolarization is introduced [20]. This means, for example, that x-polarized illumination will result in the detection of some y-polarized light upon scattering. This phenomenon suggests that polarization filtering will aid the separation of light reflected from larger objects from the light scattered by small objects, thus avoiding the complications of the double-pass nature of the optical system.

The optical system described above was modified to include an analyzer in the detection path before the pinhole of the filtered SHWFS. The extinction ratio for light measured at the SHWFS was measured as approximately 70 with a mirror specimen. Measurements were again taken using a specimen consisting of 200 nm beads in gelatin. Figures 11(e) and 11(f) show example spot patterns for this configuration. For a stationary specimen, the pupil sees a nonuniform amplitude due to speckle arising from scatter from multiple beads. Following scanning and averaging, the spot pattern forms two bands of more uniform intensity, with a dark central band. This is similar to the averaged intensity distribution found through numerical modelling of the light scattered from a single point object scanned across the focus (not shown). The resulting sensitivity and crosstalk measurements are shown in Figs. 11(g) and 11(h).

The polarization filtered results show greater variation in sensitivity between modes, when compared to the nonfiltered measurements. This is counter to expectations, but may arise from a combination of factors. First, the amount of light available for sensing is much lower in the filtered case

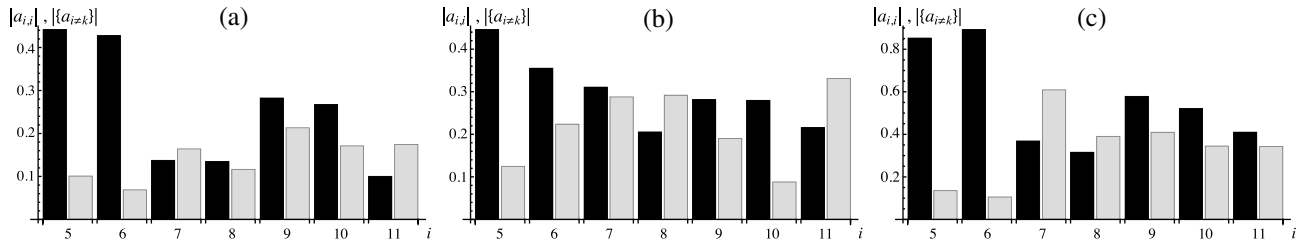

Fig. 9. Sensitivity (black) and crosstalk (gray) for Zernike modes 5 to 11 using the artificial collagen specimen with (a) 200 μm diameter pinhole, (b) 300 μm pinhole, and (c) 600 μm pinhole.

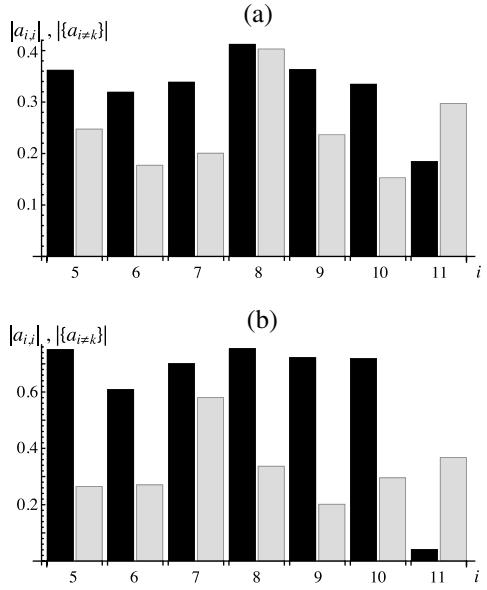

Fig. 10. Sensitivity (black) and crosstalk (gray) for Zernike modes 5 to 11 using the gold bead specimen, with (a) 300 μm and (b) 600 μm pinhole.

(<1% according to theoretical modelling). This means that the measurements are more susceptible to systematic errors due to background from elsewhere in the system. Another limitation arises from the dark pupil region, as seen in Figs. 11(e) and 11(f). In this region, the phase gradient measurements for the missing spots were replaced by a zero value. This has the effect of flattening the aberration in this region, leading to lower coefficient measurements. This reduction is worse for modes whose orientation in the pupil means that high gradients are present in this region (e.g., this affects the coma mode $i = 8$ more than coma mode $i = 7$, as these modes are rotated by 90° with respect to each other).

5. Biological Specimens

The performance of the filtered SHWFS was also investigated using biological specimens. We present here data from a *C. elegans* specimen mounted in an aqueous medium. Figure 12 shows a confocal reflection microscope image of the *C. elegans* sample. Aberration measurements were performed using light scattered back from the specimen's internal structure and filtered by a 600 μm pinhole. Symmetric and asymmetric illumination and polarization-filtered configurations were used. The compiled measurements of sensitivity and crosstalk for modes 5 to 11 are shown in Fig. 12. The response to the two coma modes ($i = 7$, 8) was found to be much less sensitive than the other low-order modes in all configurations. Neither asymmetric illumination nor polarization filtering was found to produce significant improvements in performance for this specimen. Indeed, for some modes, the measurement quality was found to decrease.

6. Discussion and Conclusion

The results show that the characteristics of the pinhole-filtered SHWFS are strongly dependent upon the specimen structure. Both the sensitivity to a given mode and the degree of crosstalk between different modes can vary. However, in many situations, the sensor does measure predominantly the induced mode, albeit with uncertain sensitivity. While this uncertainty precludes the use of this sensor in open-loop measurement, the results indicate that this method could be applied in a closed-loop correction routine. If the cross sensitivities between modes (denoted a_{ik} for induced mode i and measured mode k)

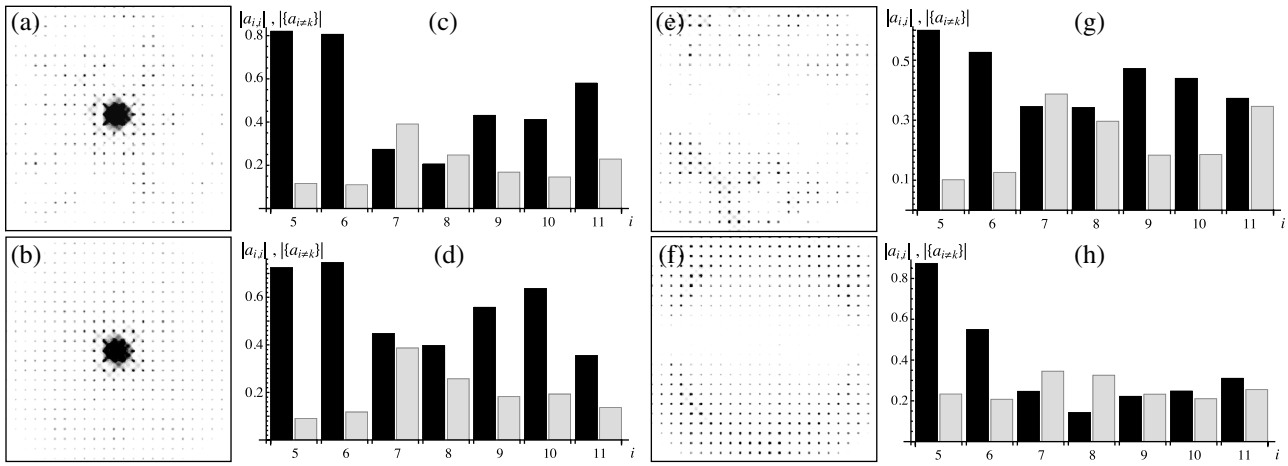

Fig. 11. Asymmetric and polarization-filtered detection. SHWFS spot patterns using asymmetric illumination and detection with the specimen of 200 nm diameter beads in gelatin: (a) stationary specimen, (b) scanned specimen with time averaging. The bright region in the center corresponds to the specular reflection component. Sensitivity (black) and crosstalk (gray) using a 300 μm diameter pinhole: (c) using symmetric illumination/detection, (d) using asymmetric illumination/detection. SHWFS spot patterns using polarization filtering: (e) stationary specimen, (f) scanned specimen with time averaging. Sensitivity (black) and crosstalk (gray) for: (g) no polarization filtering, (h) polarization filtering.

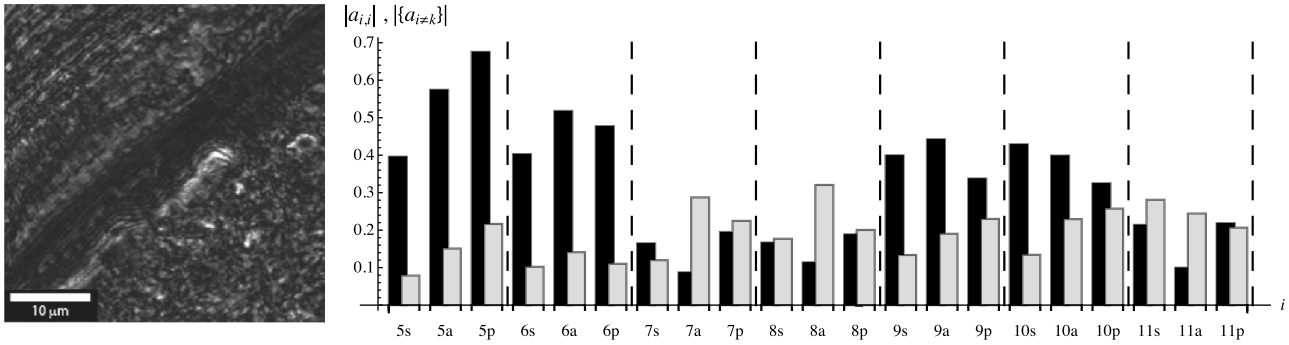

Fig. 12. Sensitivity (black) and crosstalk (gray) for Zernike modes 5 to 11 using the *C. Elegans* specimen with a 600 μm pinhole. Key: s/a, symmetric/asymmetric illumination and detection; p, polarization filtering. Image: Confocal reflection microscope image of the region of the *C. Elegans* specimen used for the aberration measurements.

are known, one can calculate the actual induced aberration. A square sensitivity matrix **S** is constructed from the elements a_{ik}, and the vectors $\mathbf{c}_{\text{actual}}$ and $\mathbf{c}_{\text{measured}}$ represent the actual induced modal coefficients and the measured coefficients, respectively. Assuming **S** is invertible, we can calculate

$$\mathbf{c}_{\text{actual}} = \mathbf{S}^{-1}\mathbf{c}_{\text{measured}}. \quad (1)$$

The degree to which uncertainty in the elements of **S** or in the measurements of $\mathbf{c}_{\text{measured}}$ can affect the calculation of actual induced aberrations is indicated by the condition number of **S**. The condition number was calculated as

$$\kappa = \|\mathbf{S}\|\|\mathbf{S}^{-1}\|, \quad (2)$$

where $\|\ldots\|$ represents the 2-norm of the matrix. Condition numbers calculated from the earlier results are compiled in Table 1. It can be seen that higher condition numbers (corresponding to ill-conditioned coefficient calculations) are seen for the cases for which some modal sensitivities were lower than the modal crosstalk, as shown in the bar charts of the earlier figures. For example, the most extreme case is for the polystyrene beads and the 200 μm pinhole, where $\kappa = 2000$. Inspection of the data in Figure 7 shows that the crosstalk exceeded the sensitivity for five of the seven modes used.

Table 1. Condition Numbers of Sensitivity Matrices Shown to Two Significant Figures[a]

Specimen	Pinhole (μm)	Configuration	Figure	Condition No.
PS beads	200	—	7	2000
PS beads	300	—	7	11
PS beads	600	—	7	4.5
Collagen	200	—	9	11
Collagen	300	—	9	8.0
Collagen	600	—	9	4.9
Gold beads	300	—	10	4.4
Gold beads	600	—	10	20
PS beads	300	symm	11	14
PS beads	300	asymm	11	3.4
PS beads	300	no polar	11	7.7
PS beads	300	polar	11	48
C. elegans	600	symm	12	3.6
C. elegans	600	asymm	12	15
C. elegans	600	polar	12	6.6

[a]Key: PS, polystyrene; symm/asymm, symmetric/asymmetric illumination and detection; polar, polarization filtering. The polystyrene beads were 200 nm diameter. The gold beads were 100 nm diameter. The figure column relates to the corresponding figure numbers in this paper.

The condition number provides a concise indicator of the likely reliability of measurements using different sensor and specimen combinations. One possible practical approach would be to estimate the matrix **S** through a sequence of measurements using the specimen region of interest. The condition number of this estimate would indicate the usefulness of closed-loop correction based upon this matrix. Further inspection of the elements of **S** could provide information about which subset of modes—those for which measurements are well conditioned—might be effectively measured and corrected. Correction of the remaining modes could be implemented using a complementary method, such as indirect optimization.

In conclusion, the results outlined in this paper illustrate the complexities of direct wavefront sensing using spatially filtered, backscattered light in adaptive scanning laser microscopes. Experimental measurements of mirror-like and point-like specimens has shown clearly that ambiguities can arise with this sensing method. The data show that absolute aberration measurements from complex scattering specimens are also ambiguous. For each of the aberration modes tested, an approximately linear relationship between the induced and detected aberration amplitude was obtained. However, the gradient of this relationship was dependent upon experimental conditions, such as pinhole diameter and scatterer density. It was also observed that the sensitivity to odd-symmetry aberration modes, such as coma, was in general lower than the sensitivity to even modes, such as astigmatism. The use of different illumination and detection apertures and polarization filtering provided improvements in some measurements, but significant benefit of these

configurations was not observed. Despite the variation of the sensitivity with specimen structure, the presence of a proportional response to the induced aberration for all modes means that this method of wavefront sensing could be used to provide a suitable feedback signal for a closed-loop correction system.

This research was supported by the Engineering and Physical Sciences Research Council, United Kingdom, grant no. EP/E055818/1.

References

1. M. J. Booth, "Adaptive optics in microscopy," Phil. Trans. R. Soc. A **365**, 2829–2843 (2007).
2. D. Débarre, E. J. Botcherby, T. Watanabe, S. Srinivas, M. J. Booth, and T. Wilson, "Image-based adaptive optics for two-photon microscopy," Opt. Lett. **34**, 2495–2497 (2009).
3. A. Jesacher, A. Thayil, K. Grieve, D. Débarre, T. Watanabe, T. Wilson, S. Srinivas, and M. Booth, "Adaptive harmonic generation microscopy of mammalian embryos.," Opt. Lett. **34**, 3154–3156 (2009).
4. J. W. Cha, J. Ballesta, and P. T. C. So, "Shack-Hartmann wavefront-sensor-based adaptive optics system for multiphoton microscopy," J. Biomed. Opt. **15**, 046022 (2010).
5. R. Aviles-Espinosa, J. Andilla, R. Porcar-Guezenec, O. E. Olarte, M. Nieto, X. Levecq, D. Artigas, and P. Loza-Alvarez, "Measurement and correction of in vivo sample aberrations employing a nonlinear guide-star in two-photon excited fluorescence microscopy," Biomed. Opt. Express **2**, 3135–3149 (2011).
6. X. Tao, B. Fernandez, O. Azucena, M. Fu, D. Garcia, Y. Zuo, D. C. Chen, and J. Kubby, "Adaptive optics confocal microscopy using direct wavefront sensing," Opt. Lett. **36**, 1062–1064 (2011).
7. P. Vermeulen, E. Muro, T. Pons, V. Loriette, and A. Fragola, "Adaptive optics for fluorescence wide-field microscopy using spectrally independent guide star and markers," J. Biomed. Opt. **16**, 076019 (2011).
8. P. Artal, S. Marcos, R. Navarro, and D. R. Williams, "Odd aberrations and double-pass measurements of retinal image quality," J. Opt. Soc. Am. A **12**, 195–201 (1995).
9. L. Diaz-Santana and J. C. Dainty, "Effects of retinal scattering in the ocular double-pass process," J. Opt. Soc. Am. A **18**, 1437–1444 (2001).
10. M. Rueckel, J. A. Mack-Bucher, and W. Denk, "Adaptive wavefront correction in two-photon microscopy using coherence-gated wavefront sensing," Proc. Natl. Acad. Sci. USA **103**, 17137–17142 (2006).
11. X. Tao, O. Azucena, M. Fu, Y. Zuo, D. C. Chen, and J. Kubby, "Adaptive optics microscopy with direct wavefront sensing using fluorescent protein guide stars," Opt. Lett. **36**, 3389–3391 (2011).
12. X. Tao, J. Crest, S. Kotadia, O. Azucena, D. C. Chen, W. Sullivan, and J. Kubby, "Live imaging using adaptive optics with fluorescent protein guide-stars," Opt. Express **20**, 15969–15982 (2012).
13. S. A. Rahman and M. J. Booth, "Adaptive optics for high-resolution microscopy: wave front sensing using back scattered light," Proc. SPIE **8253**, 82530I (2012).
14. T. Wilson, ed. *Confocal Microscopy* (Academic, 1990).
15. M. Gu, *Advanced Optical Imaging Theory* (Springer, 2000).
16. M. J. Booth, T. Wilson, H. Sun, T. Ota, and S. Kawata, "Methods for the characterization of deformable membrane mirrors," Appl. Opt. **44**, 5131–5139 (2005).
17. W. H. Southwell, "Wave-front estimation from wave-front slope measurements," J. Opt. Soc. Am. **70**, 998–1009 (1980).
18. P. Artal, I. Iglesias, N. López-Gil, and D. G. Green, "Double-pass measurements of the retinal-image quality with unequal entrance and exit pupil sizes and the reversibility of the eye's optical system," J. Opt. Soc. Am. A **12**, 2358–2366 (1995).
19. R. Navarro and M. A. Losada, "Phase transfer and point-spread function of the human eye determined by a new asymmetric double-pass method," J. Opt. Soc. Am. A **12**, 2385–2392 (1995).
20. T. Wilson, R. Juškaitis, and P. Higdon, "The imaging of dielectric point scatterers in conventional and confocal polarization microscopes," Opt. Commun. **141**, 298–313 (1997).